# Characterisation of multi-pixel superconducting nanowire single photon detectors

by

J. Swens

to obtain the degree of Bachelor of Science
at the Delft University of Technology,
to be defended publicly on Wednesday December 19, 2018 at 2:00 PM.

| | | |
|---|---|---|
| Student number: | 4226038 | |
| Project duration: | September 13, 2018 – December 12, 2018 | |
| Thesis committee: | Dr. ir. S. F. Pereira, | TU Delft, supervisor |
| | Dr. I. Esmaeil Zadeh, | TU Delft, supervisor |
| | Dr. C. Smith, | TU Delft |

An electronic version of this thesis is available at `http://repository.tudelft.nl/`.

TU Delft

# Abstract

Single-photon detection is extremely important for a number of different applications such as quantum cryptography, CMOS testing and even biomedical research. Most of the applications of single-photon detector require high efficiency combined with high time resolution, high count rates and low dark counts. Superconducting nanowire single-photon detectors has emerged provides this combination unlike any other available single-photon detectors. Some of the applications of superconducting nanowire single-photon detectors (SNSPD's) require larger area SNSPD's without affecting it's performance. For this purpose, multi-pixel SNSPD's would provide a solution. To this end, prototype 4- and 16-pixel detectors have been characterised in terms of a number of performance parameters such as critical current, count rate behaviour and timing jitter. Aside from this, simulations have been performed on detection statistics and relative illumination of the individual pixels of a multi-pixel SNSPD. Results show that for 4-pixel detectors, all desired aspects have been achieved, but not yet combined in one detector. The 16-pixel detectors showed excellent critical currents and count rate behaviour but, most likely due to the fact that they were prototype chips with little to no protection, had several not functioning pixels.

# Contents

# 1 Introduction

## 1.1. Applications of single-photon detectors

Currently, no other single-photon detectors can provide the combination of high efficiency, high time resolution, high count rates and low dark count rates that is provided by superconducting nanowire single-photon detectors (SNSPD's). Because of this, SNSPD's have a wide range of applications, such as quantum cryptography, CMOS testing, long distance communication, time-of-flight depth ranging and biomedical research. [6]
In quantum cryptography, the detectors are used for quantum key distribution. This is done by encoding data in the phase or polarisation of the photons and is a fundamentally safe way of communication. Fundamentally safe here meaning that it is theoretically impossible to intercept the communication without the other parties noticing. This fundamental safety is caused by the fact that a measurement of a quantum system will always change the state of that system.[3] [14]
In the field of electrical engineering, single photon detection is used to test and debug integrated circuit systems such as complementary metal oxide semiconductors.
Long distance communication in this case is space-to-ground communication. Efficient single photon detectors provide the possibility to send large amounts of data through laser communication with limited laser power.
In time-of-flight depth ranging, the depth of a cavity or any distance to a surface can be measured by accurately determining the time it takes a photon to go back and forth. Single photon detectors with very high time accuracy are necessary to do a useful measurement in this field.
One of the most important biomedical applications of single-photon counting is the measurement of the fluorescence lifetime of biological fluorophores. Because these fluorophores have decay times between a couple hundred picoseconds and a few nanoseconds, differences between their decay times are often in the order of 100 picoseconds. High time resolution is required to distinguish these photons from one another, and is therefore extremely important in this field.[8]

## 1.2. Multi-pixel SNSPD's

As described above, SNSPD's have applications in many different fields. This report however, is specifically about multi-pixel SNSPD's. A multi-pixel SNSPD is an SNSPD that consists of multiple nanowires. Multi-pixel SNSPD's have two main advantages over regular SNSPD's. The first main advantage is simply the possibility to detect photons with the other nanowire while one of the nanowires is in the recovery process. The second however, might be slightly less obvious. The timing jitter, which is the uncertainty in the time of arrival, depends on the length of the nanowire. Multi-pixel SNSPD's allow us to build relatively large detectors while keeping the wires short and thus keeping the timing jitter low. This is especially important in biomedical applications, where timing accuracy needs to be in the order of picoseconds.

# 2

# Theory

## 2.1. Working Mechanism

A superconducting nanowire single-photon detector (SNSPD) is a single photon detector that consists of a meandering superconducting nanowire etched from a planar thin film. When a photon hits the nanowire, it will create a local hot spot, in which the wire has no superconductivity. The current in the wire will try to avoid this non-superconducting hot spot by going around it. This will however cause the current density in the part of the wire around the hot spot to above the critical current density, causing superconduction to break down in these areas as well. At this point a "belt" has been created across the wire in which no superconduction occurs. This normal (not superconducting) part of the nanowire will have a certain non-zero resistance, causing a measurable voltage pulse. While the nanowire has non-zero resistance, it will produce heat according to $r * I^2$. This is called Joule heating. As the temperature increases, so does the resistance, causing a self-reinforcing process. After a while however, the resistance gets so high, the current is pushed into the readout circuit. This will cause the wire to cool back down to below it's critical temperature and regain superconduction. After detection the SNSPD has a certain recovery time, sometimes also called dead time, during which the wire is not in superconducting state and can therefore not detect any photons. This is illustrated in figure 2.1.

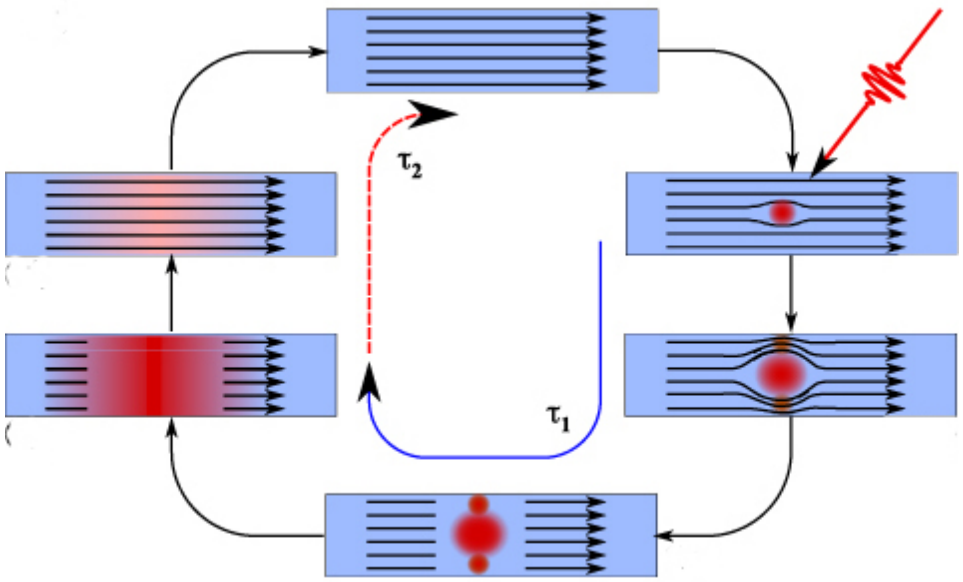


Figure 2.1: Schematic overview of the photon detection process. Adapted from "Superconducting nanowire single-photon detectors: physics and applications" by C. M. Natarajan, M. G. Tanner and R. H. Hadfield, 2012, Superconductor Science and Technology, Volume 25, Number 6.

The detectors used in this experiment consisted of a Niobium-Titanium-Nitride (NbTiN) nanowire on top of a quarter wavelength Silicon-dioxide ($SiO_2$) cavity. A gold mirror was added to increase the detection efficiency. [13]. Most SNSPD's use Niobium-Nitride (NbN) for the superconducting nanowire, but recent research has shown that NbTiN provides higher detector performance in a number of area's such as shorter recovery time, lower timing jitter and better uniformity [11].

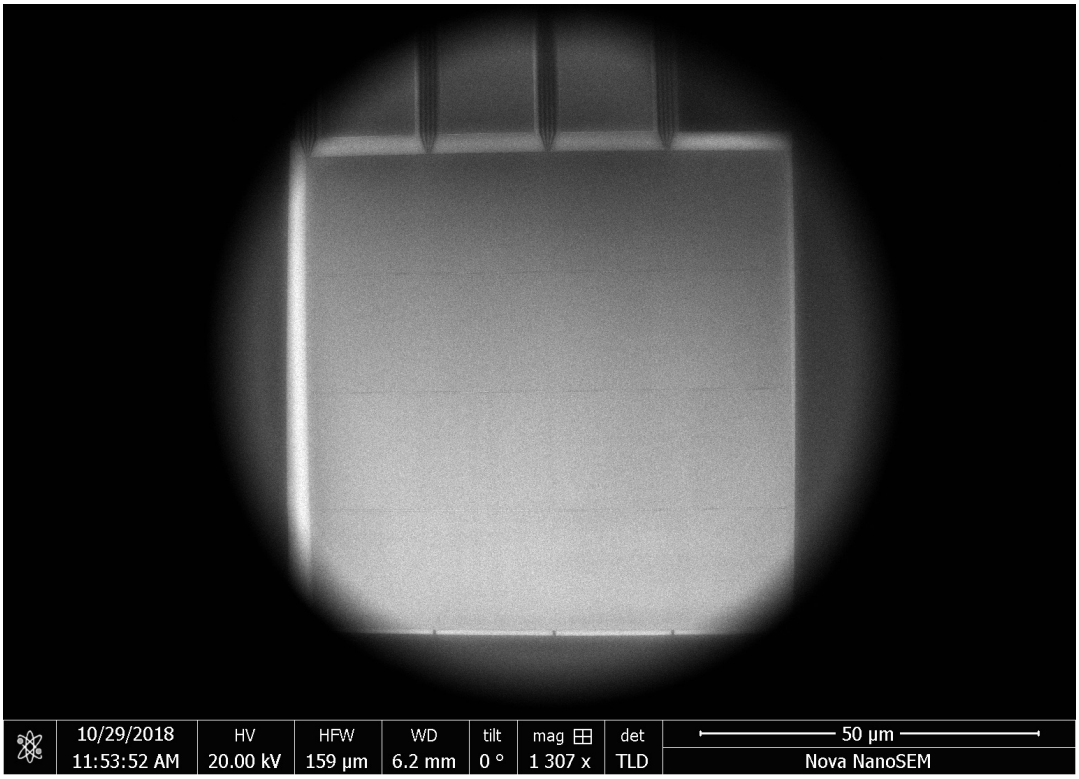


Figure 2.2: A SEM picture of a 16-pixel SNSPD.

It is also possible that a photon does not have the required energy to initiate a normal-state belt across the nanowire, but does cause a vortex crossing which will result in a normal state belt. This is called a vortex-assisted photon count. [2]. Compared to regular SNSPD's multi-pixel SNSPD's have some advantages, but also come with some extra complications. As described in section 1.2, the main advantages of this type of detector over regular SNSPD's is that the other nanowires can still detect photons while one nanowire is recovering. Another advantage is that the wires can be kept relatively short, resulting in lower timing jitter. The most important complication however, is that the readout circuit has to be altered. The current readout circuits require a coaxial cable for every pixel. This is, although impractical, possible to do for small numbers of pixels. It is not, in any case, possible to extend this process to a larger scale. As you can imagine, connecting each pixel a 1000-pixel SNSPD to it's own coaxial cable is beyond impractical, it's simply impossible. Another complication that arises from using multi-pixel detectors is that one has to prevent cross-talk. Cross-talk is the triggering of one of the pixels due to an incident photon at one of the other pixels. Since this would result in the detector counting the same photon twice, it needs to be prevented.
Two types of cross-talk could be relevant for SNSPD's: the first is radio-frequency (rf) cross-talk, and the second is thermal cross-talk. One speaks of rf cross-talk when rf signals in a wire induce other rf signals in adjacent wires. However, for the case of SNSPD's the length over which two pixels are adjacent is much shorter than the wavelength, meaning no significant amount of rf cross-talk would be expected. Thermal cross-talk however, might cause problems. Thermal cross-talk occurs when the heat generated in the part of the nanowire where the incident photon landed, spreads through the substrate and heats up an adjacent nanowire to above the critical temperature for the running bias-current.
A number of different spatial configurations can be chosen for multi-pixel SNSPD's. Three of them are displayed in figure 2.3. The left configuration is the easiest to manufacture, because it is based on dividing the a regular SNSPD into multiple pixels. It is however very sensitive to misalignment. The middle configuration, on the other hand, is not as sensitive to misalignment, but might have problems because expanding to more

pixels would cause non-uniform illumination of the pixels. The right-most configuration has neither of these problems, but would almost certainly cause too much cross-talk. Because the problem of non-uniformity seemed to be a relatively small one, the design of the middle picture was chosen for this project. Because the SNSPD's characterised in this report are of this specific configuration, in this case, the thermal cross-talk would most likely only cause a problem if the photon lands on the outermost meander of the pixel, for which the adjacent meander belongs to a different pixel. The 16-pixel version of this configuration can be seen in figure 2.2.

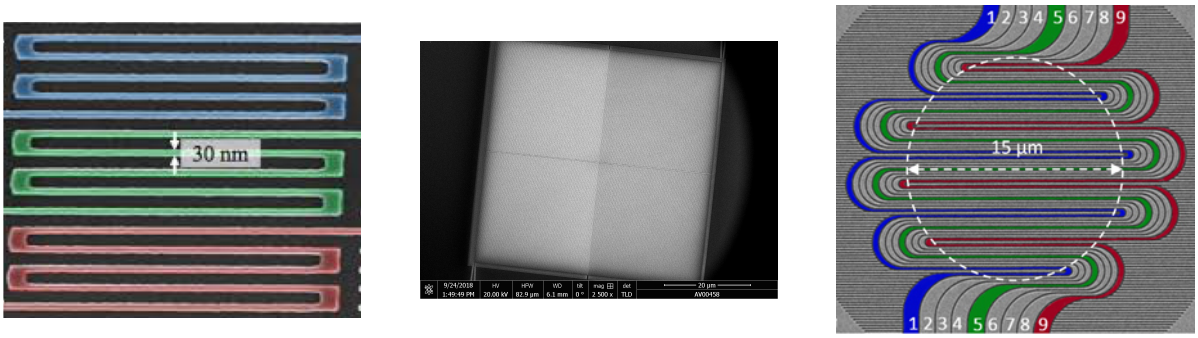


Figure 2.3: Three possible configurations for multi-pixel a detector. Left: Pixels in line. Reprinted from "Single-Photon Detectors Based on Ultranarrow Superconducting Nanowires" by F. Marsili, F. Najafi, E. Dauler, F. Bellei, X. Hu, M. Csete, R.J. Molnar and K.K. Berggren, 2011, Nano Letters, Volume 11, Number 5. Middle: 2D array of rectangular pixels. Right: Interleaved pixels. Adapted from "High speed superconducting nanowire single-photon detector with nine interleaved nanowires" by J. Huang, W. Zhang, L. You, C. Zhang, C. Lv, Y. Wang, X. Liu., H. Li and Z. Wang, 2018, Superconductor Science and Technology, Volume 31, Number 7.

## 2.2. Performance Parameters

### 2.2.1. Efficiency

The efficiency of a single photon detector is defined as the amount of detection events divided by the the total photon flux provided to the detector. Recently, detectors have been produced that reach system efficiencies of over 90% [12][7]. An issue that comes with the multi-pixel detector is that not all pixels might get the same amount of light. Therefore, in order to do proper efficiency measurements of the individual pixels uniform illumination of the detector is required.

### 2.2.2. Time Resolution

One of the most important characteristics of single photon detectors is their time resolution. This is determined by the timing jitter. Timing jitter is the variance in the amount of time it takes for the detector to generate a voltage pulse after a photon has hit the detector. To determine the jitter, a setup is created in which the arrival time of the photon is known, and measure the difference between the arrival time of the photon and the time of the signal. This is called the delay, or skew. By repeatedly performing this experiment, a histogram of the number of occurrences of a certain delay can be created. Usually, this will be a Gaussian function. The jitter is defined as the FWHM of this distribution. This is displayed in figure 4.7. As you can probably imagine, having low timing jitter is extremely important, especially in time-of-flight depth ranging. Because light travels so fast, a timing jitter of only 35 picoseconds would already result a difference in distance of 10 cm.

### 2.2.3. Count Rate

The count rate of a single photon detector is the maximum number of photons it can detect. The count rate is usually measured in Hz, and typical count rates for high-end SNSPD systems are in the order of a few hundred MHz. It should be noted that the count rate also depends on the wavelength of the measured photons. Because photons of lower wavelength have higher energy, they are more likely to trigger a normal-state band across the nanowire, causing a voltage pulse and thus a photon count. As explained in section 2.1, it is also possible to get a photon count from photons with higher wavelengths, and thus lower energy, by means of a vortex-assisted photon count.

### 2.2.4. Dark Counts

With count rate there is also dark count rate. The dark count rate is the number of counts the system produces when no light is directed to the detector. Dark counts, thus, are false counts. Dark counts are caused by spontaneous and local transitions to the normal state. These spontaneous transitions are caused by a vortex crossing the nanowire. As the vortex moves across the nanowire, it dissipates energy, thereby heating the nanowire and creating a resistive belt and thus causing a voltage pulse. [1] It is known that the vortex moves due to the Lorentz force caused by the current, but where it comes from is yet to be determined. Current theories include vortex-antivortex pair unbinding and vortex hopping at the edge of the nanowire. [10] Because the vortex is driven by the Lorentz force, it's velocity, and therefore energy, depends on the bias-current in the nanowire. This explains why higher bias-currents result in a higher dark count rate.

### 2.2.5. Recovery Time

As explained in section 2.1 the recovery time of a detector is the time it takes the detector to be able to detect a second photon after an initial detection. The recovery time is defined as the time it takes for the amplitude of the voltage pulse that was created by the detection event to go back down to $1/e$ of its maximum value. The recovery time of an SNSPD depends largely on the length versus width ratio of the nanowire. A short, thick nanowire has a much shorter recovery time than a long and thin wire. This is also why multi-pixel detectors have the potential to reach much shorter recovery times.

## 2.3. Timing jitter in multi-pixel SNSPD's

In multi-pixel SNSPD's, the timing jitter has some potentially significant contributions that do not appear in their single-pixel counterparts. The first of these contributions would be the pixel jitter. Because not all pixels are exactly identical, differences in rise-times can occur. When not all pixels have the same rise-time, the uncertainty in the time measurement increases. The second, and quite possibly most important, of the extra contributions in multi-pixel SNSPD's is the difference in readout channels, i.e. cable and wire lengths. As a rule of thumb, a signal takes about 1 ns to travel through 20 cm of coaxial cables. Because each pixel is connected to a different coaxial cable, a difference in cable length of a few hundred $\mu$m or even one mm is not unlikely. This would already add a few ps to the jitter. Aside from the coaxial cables, the pixels are all connected to the readout circuit through bonding wires. Just as with the coaxial cables, these wires may differ in length, again adding to the jitter.

# 3

# Experimental Method

In this chapter, the most important parts of the research that lead to this report will be discussed. In section 3.1, the subjects that have been simulated will be discussed. In section 3.2, the experimental set-up will be discussed, as well as the complications that arose during the experiments.

## 3.1. Simulation

### 3.1.1. Detection probability

In order to get a better feeling for the effect of the detector efficiency on the probability that all individual photons will be detected, a statistical simulation was done in Matlab®. The results of this simulation are visually represented in figure 3.1. In this simulation it was assumed that all photons arrive at the same time. This means that once a pixel has detected a photon, it cannot detect any other photons, as all of these will arrive within it's dead time. Furthermore, it was assumed that all pixels of the detectors were identical. As can be seen clearly from the figure, the importance of a high efficiency increases with the number of photons that is to be detected. For example, the probability that four photons are individually detected by a 16-pixel detector with 95% efficiency, is roughly 54%. For a detector with 80% efficiency, this would be only 28%.

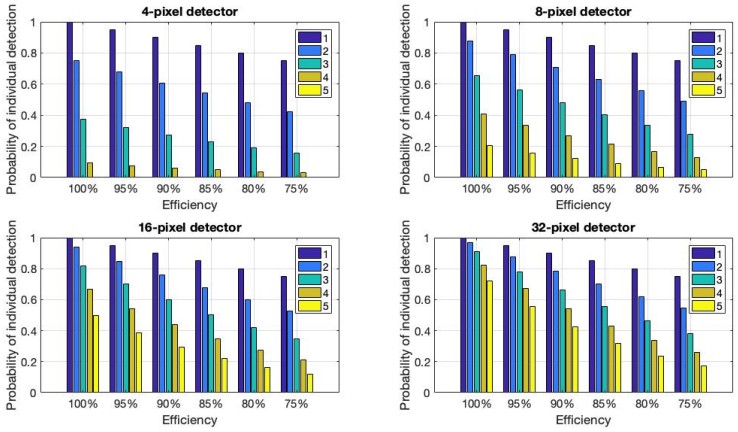


Figure 3.1: The probability that all photons will be detected individually for different pixel numbers and detector efficiencies. The vertical axis represents probability of individual detection. The horizontal axis represents the detector efficiency. The colour of the bars indicates the number of photons.

### 3.1.2. Thermal Cross-talk

As explained in section 2.1, adjacent wires of different pixels can cause cross-talk. Based on simulation by others, it was deemed very unlikely that electrical cross-talk would occur, because the adjacency of the wires is only a few micrometers, which is shorter than the wavelength of the electrical signal. Thermal cross-talk though, has not been investigated so far. Checking for thermal cross-talk through simulation simply

means checking if the heat generated by the detection event spreads far enough to cause an artificial count at the adjacent wire. In order to simulate this, the one dimensional heat equation was used. A number of finite-difference methods exist to numerically simulate the one-dimensional heat equation, such as the forward time, centred space (FTCS) method, the backward time, centred space (BTCS) method and the Crank-Nicolson method. The first two of those methods have been used during this project. The forward time, centred space method is the easiest to implement and was therefore used in the first attempts to simulate the propagation of the heat. The main problem with the FTCS method, however, is that it is not unconditionally stable. The FTCS method is only stable under the following condition:

$$\alpha \frac{\Delta t}{\Delta x^2} < \frac{1}{2}$$

, where $\alpha$ is the thermal conductivity, $\Delta t$ is the time resolution and $\Delta x$ is the spatial resolution. The value for $\alpha$ of the substrate is between 0.1 and 3 $W/(m*K)$ for the temperatures considered here [5]. The problem here is that, with $\alpha$ being of the order of a few $W/(m*K)$, one has to use attosecond time-resolution to obtain the 10 nm spatial resolution that is needed to obtain any useful information from the simulation. Running the simulation with attosecond time-resolution however, meant the created data sets would get so large no available computer could run the simulation. The other available option then, was using the BTCS method mentioned above. This method would not run into the same problems as the FTCS method because it is unconditionally stable. Using BTCS method, however, posed other problems. Because this method is a lot more complicated to implement, the code provided in [9] was used. The code provided in [9] however, was written for a different physical situation. Altering the code to fit the boundary conditions of the experiment at hand rendered this code unstable as well. After several weeks attempts still proved unsuccessful, and still no reason had been found for the instability of the BTCS scheme. It was then decided that the answer would most likely be retrievable experimentally, and that the simulation attempts would therefore be discontinued.

### 3.1.3. Relative Light Intensity

Non-uniform illumination of a multi-pixel detector can cause the different pixels to receive different light intensities, and thus a different number of photons. This happens for example when there is a slight misalignment in the fibre with respect to the centre of the detector. When working with a detector of more than 4 pixels connected to a single-mode fibre, the pixels will inevitably experience different light intensities, even when the fibre is perfectly aligned. In figure 3.2 a heat-map is displayed showing the different light intensities for different pixels of a 16-pixel detector.

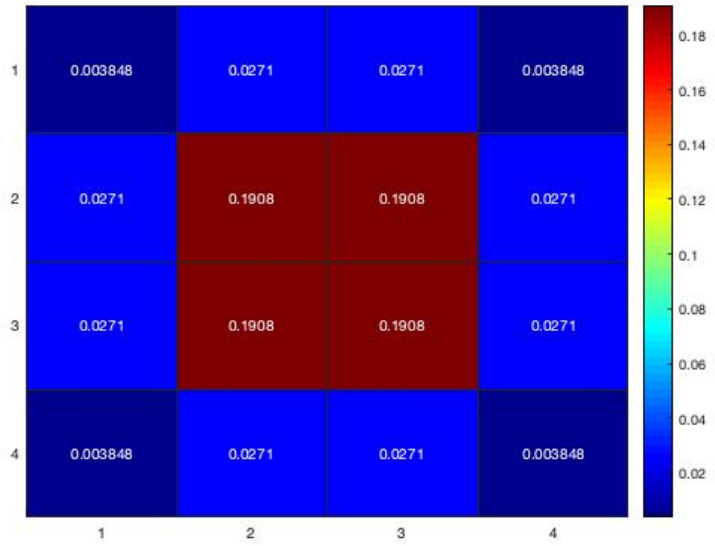


Figure 3.2: The relative light intensities experienced by the different pixels of a 16 pixel detector with 8-by-8 micron pixels connected to a single-mode fibre with a mode field diameter of 10.4 micron. The misalignment of the fibre has been averaged over all positions in a 2-by-2 micron square around the centre of the detector.

The heat-map was created by simulating the relative light intensities each pixel would receive. This was then visually represented by the colours and numbers shown in figure 3.2. The Matlab® script and function that produced the heat-map in figure 3.2 can be found in appendix B. For the characterisation of the illumination, the formula provided in figure 6 of article [4] has been slightly altered to match the conditions of the experiment. The illumination is also shown in figure B.1 in appendix B. The heat-map in figure 3.2 displays the average effect of misalignment, but the function given in appendix B can be used to create a heat-map of any desired misalignment of the fibre.

### 3.1.4. Rise time

As explained in section 2.3, the jitter in multi-pixel SNSPD's has, among others, an extra contribution from the fact that the rise time of the voltage pulse that follows a detection event might be different depending on the pixel on which the detection event occurred. One possible reason why this might be different for different pixels is a slight difference in sheet resistance. This can in turn be caused by either fabrication of the nanowire or the local properties of the superconducting film itself. In order to create a better understanding of the effects of a difference in sheet resistance, the rise time was simulated as a function of the sheet resistance. In order to perform this simulation, the output voltage of the detector was simulated for five different values for the sheet resistance. The results of this simulation are visually represented in figure C.1 in appendix C. These results were then used to calculate the rise time for each value of the sheet resistance. These rise times have been plotted as a function of the sheet resistance in figure 3.3.

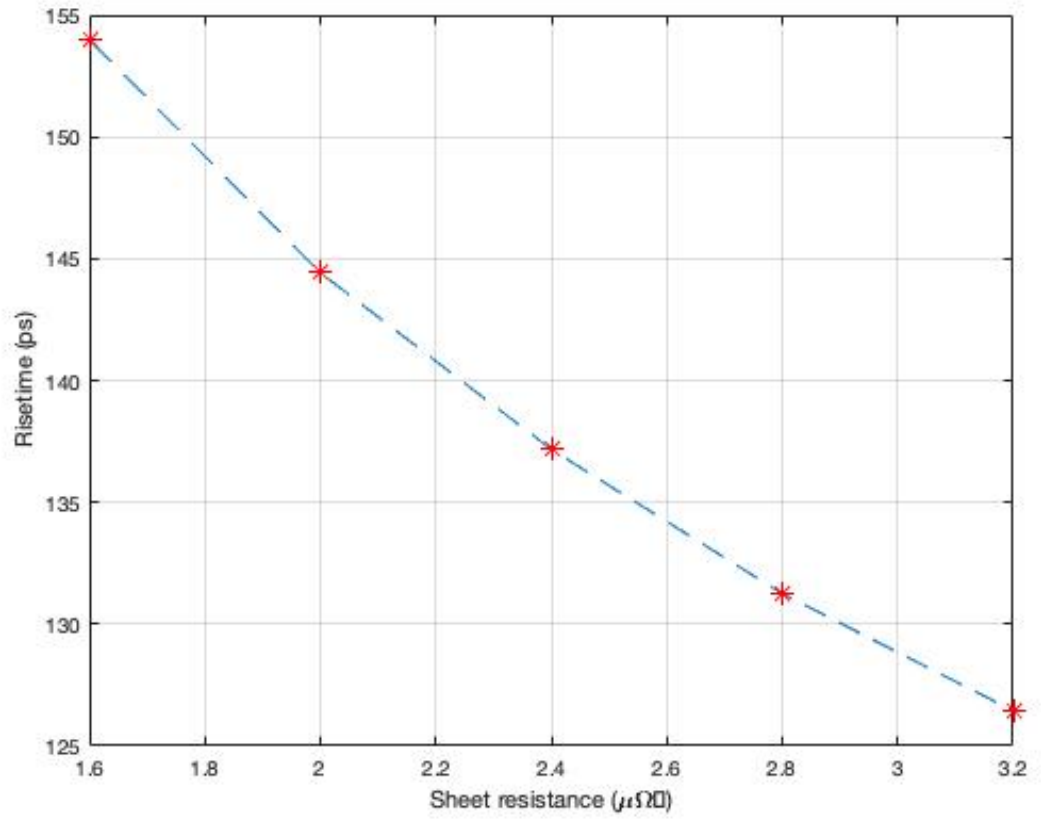


Figure 3.3: The rise time of the voltage pulse of a single pixel of an SNSPD as a function of the sheet resistance. For this simulation, a film thickness of 4 nm was chosen. The nanowire was 100 nm wide and 1.5 $\mu$m long. The bias current was chosen to be 16.5 $\mu$A, a few $\mu$A under the critical current of 20$\mu$A. The nanowire was chosen to have a critical temperature of 10.5 K, with the substrate at 2 K.

## 3.2. Measurements

In order to characterise the SNSPD's, several detectors were tested. To accurately determine the exact value of all of the performance parameters, one needs to perform the measurements on a fibre-coupled detector placed in a cryostat. The cryostats used in this report are Gifford-McMahon cryostats running on compressed helium. The in- and outside of such a Gifford-McMahon cryostat is shown in figures 3.4 and 3.5 respectively. Unfortunately, not all measurements could be performed in such an environment. Because most of the tested detectors were prototype chips, only a few of them could be mounted on a printed circuit board (PCB) which allowed fibre-coupling. Other detectors were tested under flood illumination. Thankfully, the only parameter of the detector that is affected by the fact that it is not fibre-coupled is the efficiency. However, because not enough measurements have been done on fibre-coupled detectors to obtain any significant data, the efficiency will not be discussed any further.

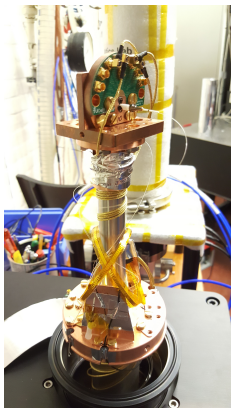

Figure 3.4: A fibre-coupled detector mounted in a cryostat.

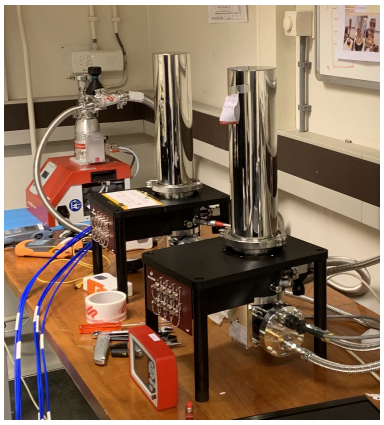

Figure 3.5: The outside of a cryostat.

Some of the 4-pixel and both of 16-pixel detectors however, were mounted on PCB's that could not be mounted in a cryostat. Such a PCB is shown in figure 3.6. These measurements were therefore performed using a dipstick, which is shown in figure 3.7, in a tank of liquid helium instead of the compressed helium used in the closed-cycle cryostat. Given that the temperature of liquid helium is almost 2 K higher than that of the compressed helium in the cryostat, the detector performance will be slightly lower in this environment. This will be noticeable especially for the critical current and the saturation of the detectors.

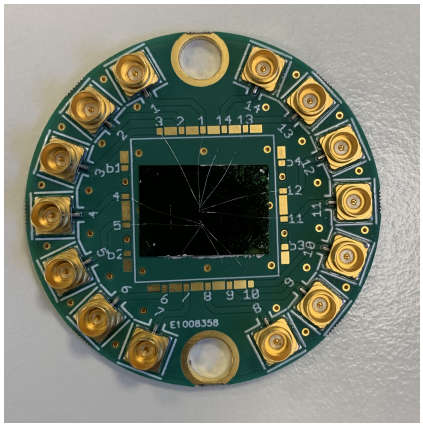

Figure 3.6: A PCB with a wire-bonded detector. The circuit board is used to read out the detector and attach it to a dipstick.

Figure 3.7: A dipstick after measurement. The dipstick has just been removed from a container of liquid helium and at the bottom the PCB is still attached.

# 4

# Results

## 4.1. 4-pixel detectors

The 4-pixel detectors tested for this paper were tested in one of the three available setups: flood illumination in liquid helium, flood illumination in a cryostat or in a cryostat with individual fibre-coupled devices. As expected, the detectors measured in liquid helium showed significantly less saturation and lower critical currents.

### 4.1.1. 4-pixel detectors in liquid helium

The first of the tested 4-pixel detectors showed two pixels working normally, one pixel not working at all, and one pixel producing counts but showing no critical current. Most likely the bonding wire of the pixel showing no superconduction had accidentally been connected to ground. The IC-curves of the two working channels can be found in figure D.1 in appendix D. The second detector showed significantly better results, with three pixels working as expected. With 2 of the pixels having high, and identical critical currents, results of the IV-curves were promising. Aside from the IV-curves, IC-curves were measured for dark count rate (DCR) and under illumination for two different wavelengths. The IC-curves of the detector under illumination are shown in figure 4.1. Other IV-curves and dark count IC-curves can be found in appendix D in figures D.2 and D.3 respectively.

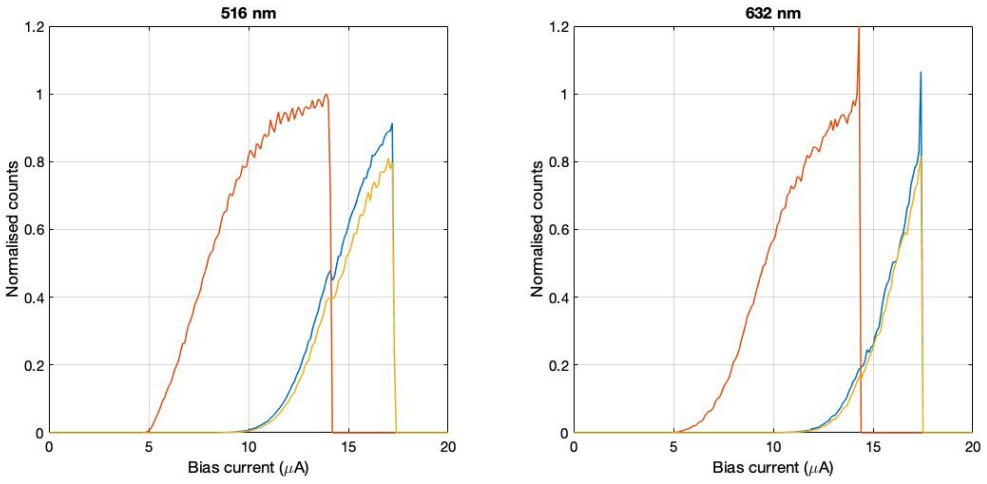


Figure 4.1: The IC-curves of the three working pixels of the second 4-pixel detector that was tested in liquid helium. The different colours correspond to the different pixels. The detector was tested for two wavelengths: 516 nm (left) and 632 nm (right). The counts have been normalised to the highest overall count rate.

### 4.1.2. 4-pixel detectors in a closed-cycle cryostat

Three detectors have been tested in while fibre-coupled, but only one of them showed any usable results. For the other two, the critical currents of the different pixels were too far apart and the count rate behaviour was different for each pixel. The other detector showed much better results. Critical currents were, exactly identical at 11.8 $\mu$A, and all four pixels worked. The IC-curves of this detector are plotted in figure 4.2. As can be seen from the figure, the behaviour of the curves is very different. This difference, however, can most likely be attributed to non-uniform illumination. This also caused a very large difference in count rates, with the highest count rate of the most illuminated pixel being almost 350 times as high as that of the least illuminated pixel. This non-uniformity was most likely the result of a fabrication error, causing the pixels to be not in line with the fibre.

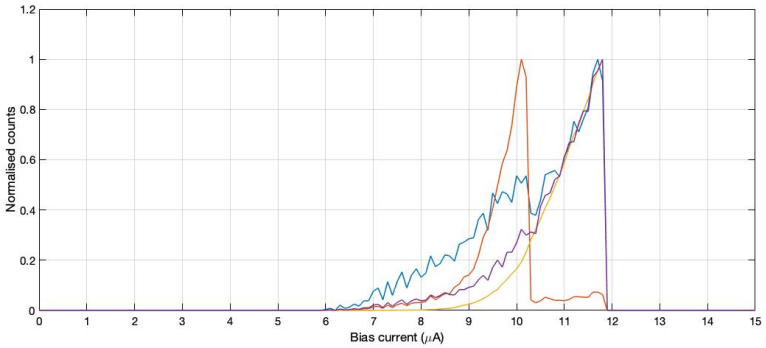


Figure 4.2: The IC-curves of the good 4-pixel detector that was tested while fibre-coupled in a closed-cycle cryostat. Because of the large difference in count rates between the pixels, the pixels have been normalised individually.

Aside from the three detectors tested while fibre-coupled, one detector was tested in a cryostat under flood illumination. Despite having only three working pixels, this detector showed very good results. The three working pixels had high (over 20 $\mu$A) critical currents, all within 1 $\mu$A of each other, and their count rate behaviour was almost identical. Furthermore, all pixels showed very good saturation at 780 nm. The IC-curves of this detector have been plotted for two different wavelengths in figure 4.3.

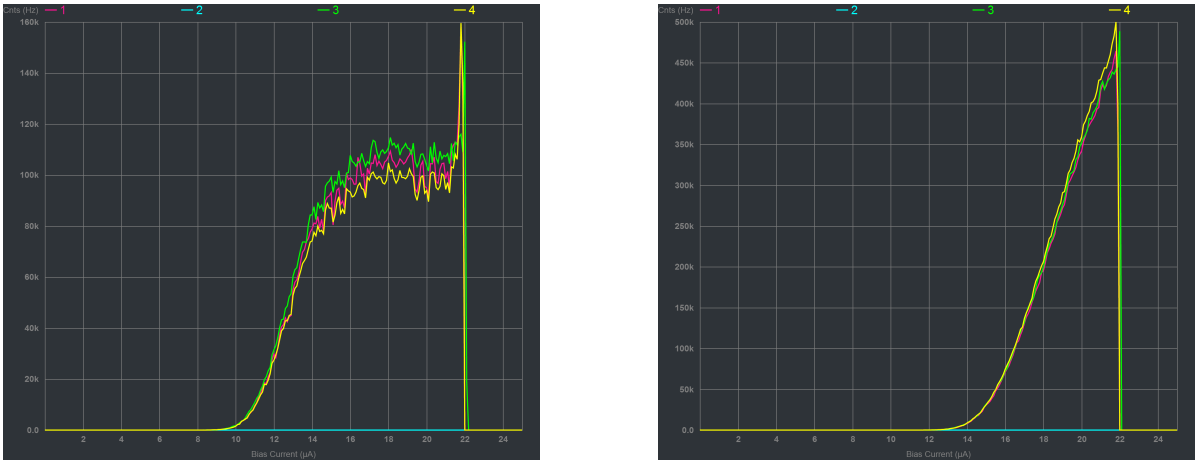

Figure 4.3: The IC-curves of a 4-pixel SNSPD in a cryostat under flood illumination by laser light with a wavelength of 780 nm (left) and 1300 nm (right). The different colours correspond to the different pixels. Three out of four pixels work. The vertical axis represents the number of counts. The horizontal axis represents the bias current.

## 4.2. 16-pixel detectors

For this report, two 16-pixel detectors have been tested. As mentioned in section 3.2, the 16-pixel detectors were, for practical reasons, tested in liquid helium. Because liquid helium has a slightly higher temperature,

this had a negative effect on a number of parameters such as the critical current and the saturation of the internal efficiency of the detector. Because of physical complications and the way the detectors are designed, it is not possible to bond more than 11 detectors at a time. For both of the detectors then, 11 pixels have been tested. As was the case with 4-pixel detectors, not all pixels of the 16-pixel detectors worked. One of the detectors showed 4 out of 11 working pixels, the other one was slightly better, showing 6 out of 11 working detectors. Ideally, one would want all pixels to show exactly the same behaviour, so no computational corrections would be required to gather usable data from the detector. The detector with 4 working pixels already showed promise, as all 4 pixels had their critical current in a 1 $\mu$A range. Also their count rates behave fairly similar. This can be seen in figure 4.4.

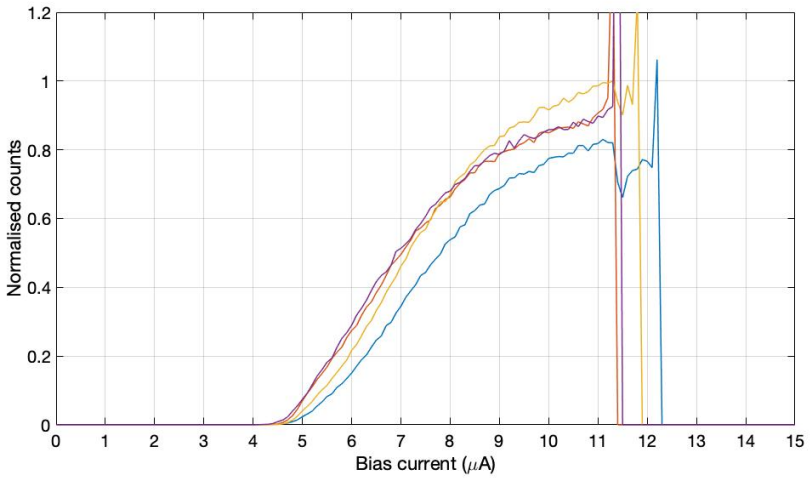


Figure 4.4: The IC-curves of the 4 working pixels of one of the 16-pixel detectors. The different colours correspond to the different pixels.

The second detector that was tested showed not only more working pixels, but also better behaviour of those pixels. As can be seen from the IC-curves in figure 4.5, the critical current of all 6 pixels is exactly the same, and their behaviour under illumination almost identical. The difference in count rates between the pixels can be explained by the fact that not all pixels get the same illumination, as explained in section 3.1.3.

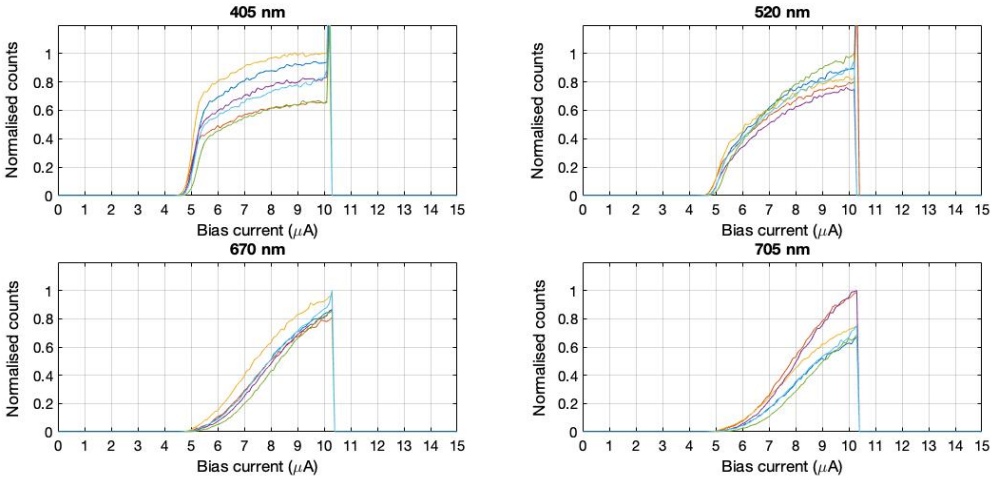


Figure 4.5: The IC-curves of the detector with 6 working pixels for 4 different wavelengths. The different colours correspond to the different pixels.

As can be seen from the IC-curves for 670 nm and 705 nm in figure 4.5, the detector currently does not show very much saturation at higher wavelengths; this will, however, improve when measured at lower temperatures, such as in a closed-cycle cryostat. The fact that different pixels show the highest count rate for different wavelengths is due to a difference in illumination pattern. The fibre used in these experiments is,

for wavelengths below roughly 1300 nm, a multi-mode fibre. This means that the illumination pattern of the fibre changes with wavelengths. This will result in different pixels getting the highest light intensity for different wavelengths. Aside from their count rates and critical current, for all pixels the rise times (20%-80%) of their voltage pulses and dead their times were measured. For all pixels the measured rise-time was between 465 and 500 ps, and the dead time was between 31 and 33 ns. The voltage pulse of 5 of the pixels has been plotted in figure 4.6.

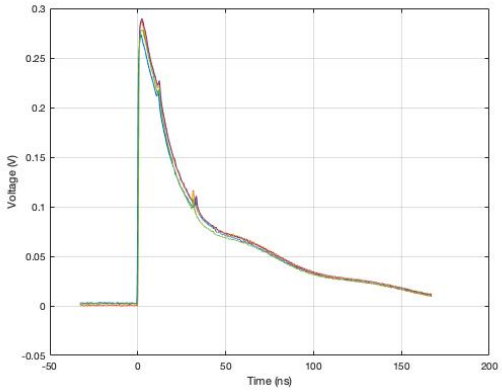


Figure 4.6: The voltage pulses of the detector. The figure shows the pulse created by a detection event. The different colours correspond to the different pixels. The vertical axis represents the voltage. The horizontal axis represents the time.

For 2 of the pixels, the timing jitter was measured as well, as is shown in the bar graph in figure 4.7.

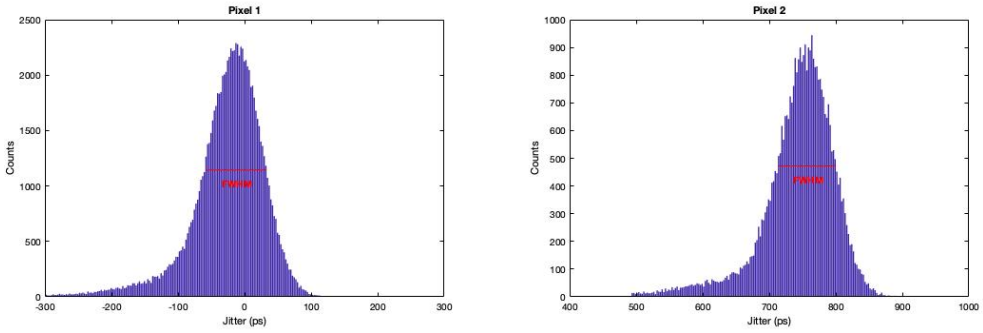


Figure 4.7: Bar graphs of the jitter of 2 of the pixels of the 16-pixel detector. The timing jitter of pixel one is 90 ps, that of pixel two is 85 ps. The vertical axis represents the number of occurrences. The horizontal axis represents the skew.

The fact that the jitter shown in figure 4.7 is significantly higher than the jitter measured in some of the single-pixel detectors (of less than 10 ps [13]) at the same facility can be attributed to a number of factors. As with most other performance parameters, the jitter will improve with decreasing temperature, and will therefor be lower when tested in a compressed helium cryostat. Another explanation is the pixel jitter and difference in cable length, as discussed in section 2.3. In the experiments performed here, however, the bonding wires connecting the pixels to the PCB differed in length by as much as 5 mm. This factor alone would add up to 25 ps to the jitter.

# 5

# Conclusions and recommendations

## 5.1. 4-pixel detectors

Based on the experiments performed and the results obtained, one can say that, in almost all cases, the tested detectors showed expected behaviour in some areas but rarely in all areas. The detectors of which all four pixels worked, often had differing or very low critical currents or large differences in count rate behaviour. The detectors that showed similar, high critical currents and almost identical count rate behaviour on the other hand had only two or three working pixels. All in all one can say that all desired aspects of a 4-pixel detector have been obtained, but never all in the same detector. Most likely detectors will be fabricated in the near future that will combine these desirable aspects. Everything that is required to fully characterise a 4-pixel detector, including for example efficiency measurements, is readily available. It seems than, that the main challenge lies in the fabrication of the detectors.

## 5.2. 16-pixel detectors

The experiments performed for this report could not provide detailed characterisation of all aspects of a 16-pixel detectors. Reasons for this include the fact that only 11 pixels could be bonded at once, and no cryostats were available to cool the detectors down far enough to obtain maximum performance. The detectors that were tested did show promising results in the area's that could be characterised at this time. It is clear however, with both 16-pixel detectors showing no more than 55% of the pixels working, that the fraction of the pixels that work is significantly lower in the 16-pixel detectors than it is in the 4-pixel detectors. The behaviour of the pixels that do work, however, is excellent. It seems, then, as the pixels that do work already show very good behaviour, that improvements on the 16-pixel detector should focus almost solely on increasing the fraction of working pixels. For further research, possibilities should be explored to bond all 16 pixels at the same time. Also a cryostat should be modified to offer the possibility of fibre-coupling a 16-pixel detector. Only once these steps have been made, will it be possible to fully characterise all aspects of the 16-pixel detector.

# Acknowledgements

This report would not have been possible without the help of others. First of all I would like to thank my supervisors, Iman Esmaeil Zadeh and Silvania Pereira for helping me in the writing process. Extra thanks go out to Iman for explanation of the subject matter and the fabrication of the detectors. Furthermore special thanks go out to Jin Chang for bonding the detectors repeatedly helping with the measurements. Lastly I would like to thank Monique Gevers and other people at Single Quantum for helping with the measurements and answering any questions I had at that time.

# A

# Detection Statistics

The following Matlab® function calculates the probability of individual detection for different number of detectors, number of photons and detector efficiencies. It also produces the bar graphs shown in figure 3.1.

```
function[p,g] = detectstat(n,c,emin,emax,estep)

%input:
    %n = number of photons
    %c = number of detectors (can be array)
    %emin = minimum detector efficiency
    %emax = maximum detector efficiency
    %estep = step in detector efficiency

%output
    %p = probability of indidual detection of all photons
    %g = bar graph of p

f = 1:n;
e = emin:estep:emax;

for i = 1:numel(f);
     for j = 1:numel(c);
         for k = 1:numel(e)
             if c(j)-f(i) ≥ 0;
                 p(i,j,k) = ...
                     e(k).*((e(k)./c(j))^(f(i)-1))*factorial(c(j)-1)/factorial(c(j)-f(i));
             else
                 p(i,j,k) = 0;
             end
        end
    end
end

for k = 1:numel(e);
    subplot(1,numel(e),numel(e)+1-k,'align')
    bar(f,p(:,:,k))
    axis([0.5 5.5 0 1])
    titlecell = cellstr(num2str(100.*e(k)', '%-d%% efficiency'));
    title(titlecell)
    xlabel('Number of photons')
    ylabel('Probability of individual detection')
    legendcell = cellstr(num2str(c', '%-d'));
    legend(legendcell)
    grid ON
end
end
```

# B

# Relative Light Intensity

The Matlab® function listed below calculates the relative light intensities for different pixels and different misalignment of the optical fibre.

```
function[e,Etot,Enorm,h] = Misalignment(simsize,step,psize,n,dx,dy,mfd)

%input:
    %simsize = distance from the center to the edge of the simulation area
    %step = stepsize in micrometers
    %psize = pixelsize in micrometers
    %n = number of pixels
    %dx = misalignment in x direction
    %dy = misalignment in y direction
    %mfd = mode field diameter of fiber

%output:
    %e = the relative amount of light received by each pixel
    %Etot = the relative amount of light received by all pixels together
    %Enorm = the normalised relative amound of light received by each pixel
    %h = heatmap of e


[x y] = meshgrid(-simsize:step:simsize);
pixelsize = 10*psize;
mid = length(x)/2;
detectorsize = sqrt(n).*pixelsize;
leftedge = mid-0.5*detectorsize;
bottomedge = mid-0.5*detectorsize;

I = exp(-2.*(sqrt((x-dx).^2+(y+dy).^2)./mfd).^2);
TotI = sum(I(:));

for i = 1:sqrt(n)
    for j = 1:sqrt(n)
        e(i,j) = sum(sum(I((leftedge+(i-1)*pixelsize+1):(leftedge+i*pixelsize),
        (bottomedge+(j-1)*pixelsize+1):(bottomedge+j*pixelsize))))/TotI;
    end
end

h = heatmap(e,'Colormap',jet);

Etot = sum(e(:));
Enorm = e./max(e(:));
end
```

The Matlab® code below uses the Misalignment function listed above to calculate the relative light intensities for the different pixels averaged over different misalignment positions positions in a 2-by-2 micrometer square.

```
for i = 1:101
    for j = 1:101
        [E(:,:,i,j)] = Misalignment(49.95,0.1,8,16,(i-51)/50,(j-51)/50,10.4);
    end
end

meanE = mean(mean(E,3),4);

h = heatmap(meanE,'Colormap',jet)
```

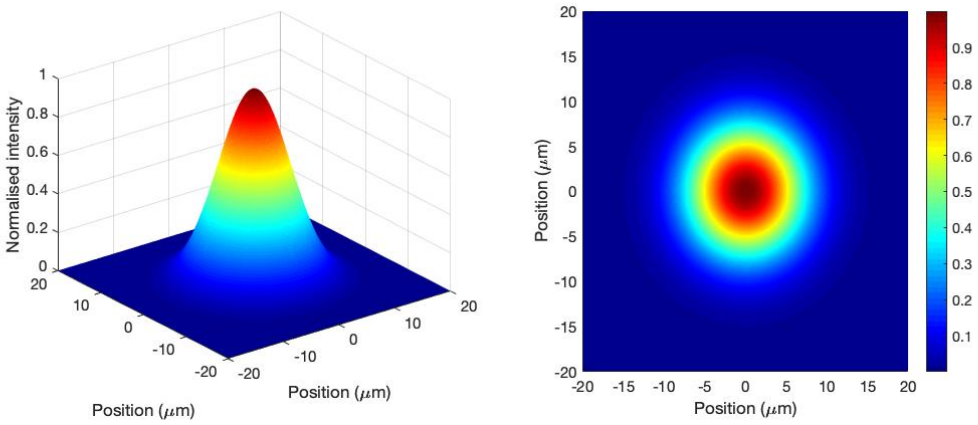


Figure B.1: The relative intensity of the the beam of light at the end of a SMF 28 fibre with an MFD of 10.4 $\mu$m.

# C

# Rise Time

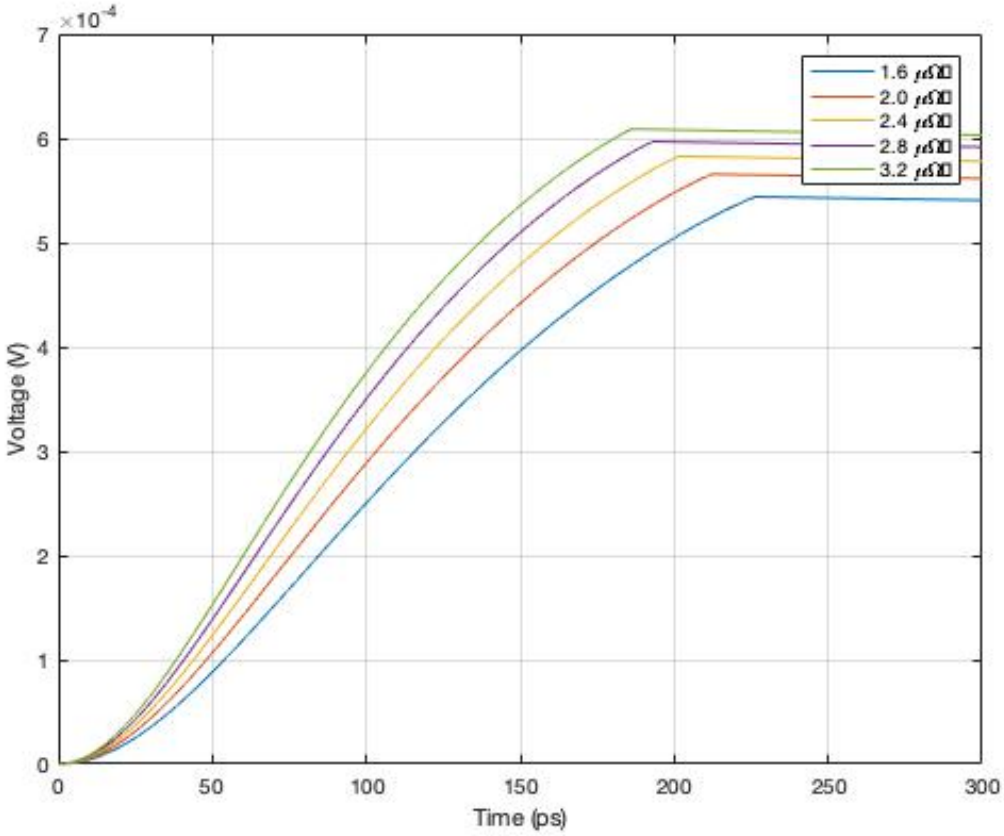


Figure C.1: A simulation of the rise of voltage pulse generated single pixel of an SNSPD plotted for five different values of the sheet resistance. For the simulation the same parameters were used as in figure 3.3.

# D

# Detector Data

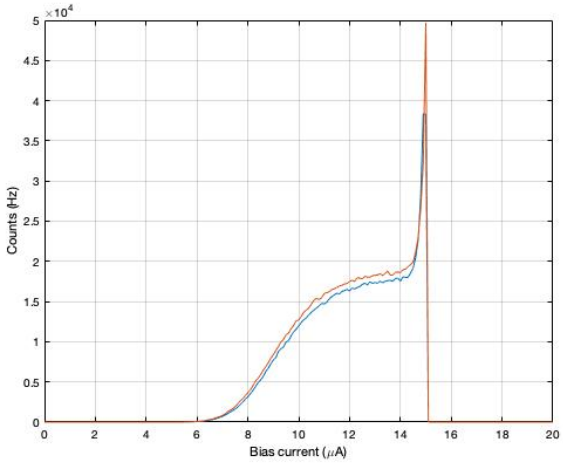


Figure D.1: The IC-curve of the 2 working pixels of the first 4-pixel detector, measured in liquid helium. The vertical axis represents the number of counts. The horizontal axis represents the bias current.

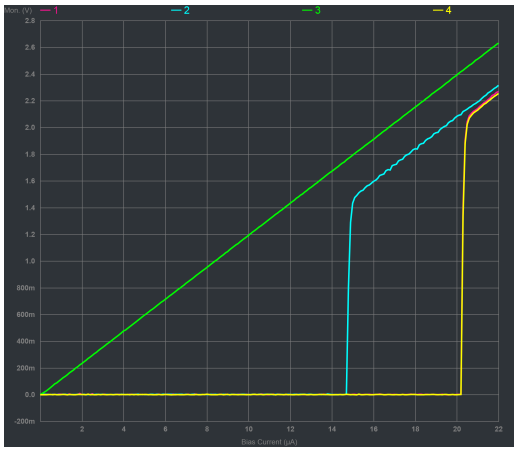

Figure D.2: The IV-curves of the second 4-pixel detector, measured in liquid helium. The vertical axis represents the voltage. The horizontal axis represents the bias current.

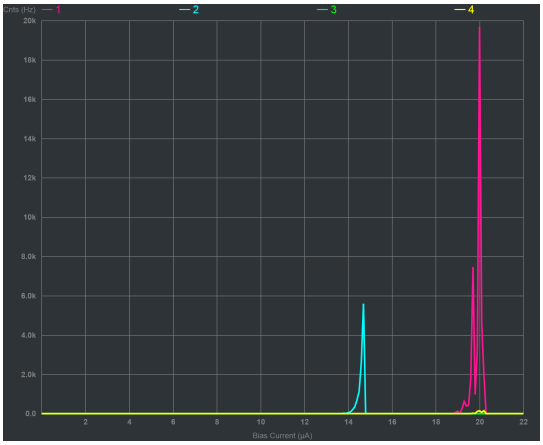

Figure D.3: The dark count IC-curves of the second 4-pixel detector, measured in liquid helium. The vertical axis represents the number of counts. The horizontal axis represents the bias current.

# Bibliography


[1] L. N. Bulaevskii, M. J. Graf, and C. D. Batista. Vortex-induced dissipation in narrow current-biased thin-film superconducting strips. *Physical Review*, 83:144526, 2011. doi: 10.1103/PhysRevB.83.144526.

[2] L. N. Bulaevskii, M. J. Graf, and V. G. Batista. Vortex-assisted photon counts and their magnetic field dependence in single-photon superconducting detectors. *Physical Review*, 85:014505, 2012. doi: 10.1103/PhysRevB.85.014505.

[3] Y. Gisin, G. Ribordy, W. Tittel, and H. Zbinden. Quantum cryptography. *Reviews of Modern Physics*, 74:145–190, 2002. doi: 10.1103/RevModPhys.74.145.

[4] A.M. Kowalevicz Jr and F. Bucholtz. Beam divergence from an smf-28 optical fiber. *Naval Research Laboratory*, 2006. doi: https://apps.dtic.mil/dtic/tr/fulltext/u2/a456331.pdf.

[5] J.C. Lasjaunias, A. Ravex, M. Vandorpe, and S. Hunklinger. The density of low energy states in vitreous silica: Specific heat and thermal conductivity down to 25 mk. *Solid State Communications*, 88(11):1023 – 1027, 1993. doi: 10.1016/0038-1098(93)90288-X.

[6] Y. Liang and H.P. Zeng. Single-photon detection and its applications. *Science China: Physics, Mechanics & Astronomy*, 57:1218–1232, 2014. doi: 10.1007/s11433-014-5450-0.

[7] F. Marsili, V. B. Verma, J.A. Stern, S. Harrington, A. E. Lita, T. Gerrits, I. Vayshenker, B. Baek, M. D. Shaw, R. P. Mirin, and S. W. Nam. Detecting single infrared photons with 93% system efficiency. *Nature Photonics*, 7:210 EP –, 02 2013. doi: /10.1038/nphoton.2013.13. URL `https://doi.org/10.1038/nphoton.2013.13`.

[8] D. Palubiak, M. M. El-Desouki, O. Marinov, M. J. Deen, and Q. Fang. High-speed, single-photon avalanche-photodiode imager for biomedical applications. *IEEE Sensors Journal*, 11:2401–2412, 2011. doi: 10.1109/JSEN.2011.2123090.

[9] G.W. Recktenwald. Finite-difference approximations to the heat equation. *Mechanical Engineering*, 10, 2004.

[10] T. Yamashita, S. Miki, K. Makise, W. Qiu, H. Terai, M. Fujiwara, M. Sasaki, and Z. Wang. Origin of intrinsic dark count in superconducting nanowire single-photon detectors. *Applied Physics Letters*, 99:161105, 2011. doi: 10.1063/1.3652908.

[11] X. Yang, L. You, L. Zhang, C. Lv, H. Li, X. Liu, H. Zhou, and Z. Wang. Comparison of superconducting nanowire single-photon detectors made of nbtin and nbn thin films. *IEEE Transactions on Applied Superconductivity*, 28(1):1–6, 2018. doi: 10.1109/TASC.2017.2776288.

[12] I. Esmaeil Zadeh, J. W. N. Los, R. B. M. Gourgues, V. Steinmetz, G. Bulgarini, S. M. Dobrovolskiy, V. Zwiller, and S. N. Dorenbos. Single-photon detectors combining high efficiency, high detection rates, and ultra-high timing resolution. *APL Photonics*, 2(11):111301, 2017. doi: 10.1063/1.5000001. URL `https://doi.org/10.1063/1.5000001`.

[13] I. Esmaeil Zadeh, J.W. N. Los, R. Gourgues, G. Bulgarini, S.M. Dobrovolskiy, V. Zwiller, and S.N. Dorenbos. A single-photon detector with high efficiency and sub-10 ps time resolution, 01 2018.

[14] C. Zhou, G. Wu, X. Chen, H. Li, and H. Zeng. Quantum key distribution in 50-km optic fibers. *Science China: Physics, Mechanics & Astronomy*, 47:182–188, 2004. doi: 10.1360/03yw0094.